

Annealing time, temperature, and field dependence of pinned magnetic moments in the collinear antiferromagnet PdMn

Nicolas Josten,* Olga Miroshkina, Mehmet Acet, Markus Gruner, and Michael Farle
*Faculty of Physics and Center for Nanointegration (CENIDE),
 University Duisburg Essen, Duisburg, 47057, Germany*

(Dated: March 7, 2023)

Magnetic annealing of the collinear antiferromagnet PdMn with excess Pd produces strongly pinned magnetic moments in the annealing field direction. This behaviour can be understood with the help of the magnetic-field-biased diffusion model. Here, the magnetic field creates an energy difference between the two possible occupations of the antiferromagnetic Mn-sublattices by the Pd-excess atoms. This, mediated by diffusion, leads to an imbalance in the amount of the Pd-excess atoms in these sublattices and, subsequently, to an imbalance in the total magnetization of the sublattices. We investigate this effect's dependence on the annealing field, time, and temperature. The results are then compared to the results of the magnetic-field-biased diffusion model, which gives good agreement.

I. INTRODUCTION

Mn and its alloys are known for their versatile and interesting magnetic properties. These include the complex magnetism of manganese in allotropic forms [1, 2], spin-glasses (e.g. Cu-Mn) [3], and Heusler alloys (e.g. Cu₂MnAl) [4]. Another class of Mn-alloys are the collinear antiferromagnets IrMn, PdMn, PtMn, NiMn, and RhMn, which have a tetragonal L1₀-structure and are often used as the pinning layer in exchange biased films [5, 6].

It was shown that annealing NiMn with up to 5% excess Ni under a magnetic field leads to the formation of strongly pinned uncompensated magnetic moments [7]. This effect manifests itself as a shift along the magnetization axis in the magnetic field dependence of the magnetization $M(B)$. The mechanism is thought to be related to magnetic-field-biased diffusion [7, 8]. Excess Ni-atoms have to occupy Mn-positions. Since NiMn is a collinear antiferromagnet, excess Ni has to occupy one or the other of the two antiferromagnetic (AF) sublattices, which results in locally induced magnetic moments. During magnetic annealing under an annealing field (B_a) applied in a given direction, the occupation of one of these sublattices is energetically more favorable for the excess Ni-atoms. This leads to an imbalance in the distribution among the sublattices and subsequently to a net magnetization.

In certain cases, Pd can have a ferromagnetic (FM) coupling with its environment [9, 10]. Therefore, it can be expected that excess Pd exhibits FM ordering induced by a Mn environment in Pd-rich PdMn as excess Ni does in Ni-rich NiMn.

PdMn around the equiatomic composition transforms martensitically between a high-temperature B2 phase and a low-temperature L1₀ phase [11]. At the equiatomic composition, the transition temperature is about 900 K [11–13]. The L1₀ phase of PdMn is a collinear an-

tiferromagnet, and its Néel temperature lies around 820 K [13–15]. At the equiatomic composition, only the Mn atoms carry a magnetic moment, which is around $4 \mu_B$ found in the results of both experimental [13, 14] and *ab initio* theoretical studies [16, 17]. The magnetic easy-axis lies within the c-plane [14], and the calculated magnetocrystalline anisotropy constant is $K_2 = -1.53 \times 10^6 \text{ J m}^{-3}$ [18].

The aim of this work is to show that magnetic annealing of PdMn with excess Pd leads to local FM coupling and pinning of the magnetization along B_a . For this, we present the dependencies of the amount of pinned magnetization on B_a , the annealing time (t_a), and the annealing temperature (T_a) and use the magnetic-field-biased diffusion model to describe the results.

II. METHODS

A. Experimental

PdMn with excess Pd was prepared by arc melting of pure elements (99.98%). The sample was homogenized for 5 days at 1073 K encapsulated in a quartz tube under argon atmosphere. Afterwards, it was quenched in water at room temperature. We used energy-dispersive X-ray spectroscopy (EDX) incorporated in a scanning electron microscope and determined the composition as Pd_{52.9}Mn_{47.1}. The sample was cut into disks with ~ 1 mm thickness using a precision sectioning saw. X-ray diffraction (XRD) measurements were carried out using Cu K- α radiation. Each disk was cut into multiple cuboids ranging from 19.9 mg to 59.7 mg for magnetization measurements. Additional grinding removed any cutting residues.

The magnetic properties were measured in a Quantum Design MPMS XL superconducting quantum interference device (SQUID) magnetometer with a high-temperature unit. First, a 5 T- $M(B)$ -curve at 300 K was taken for an initial state sample. The field was then set to the value

* Nicolas.Josten@uni-due.de

of B_a and warmed to T_a at a rate of 4 K min^{-1} . The sample remained at this temperature for a chosen time and subsequently cooled back to 300 K at the same rate without removing the field. Afterwards, $M(B)$ was measured again at 300 K. $M(B)$ at 300 K of the annealed state shows a vertical shift with respect to $M(B)$ of the initial state (as-prepared). This procedure was repeated for various B_a , t_a , and T_a to understand the mechanisms behind the occurrence of the vertical shift. A fresh sample was used for each B_a and T_a . For the t_a -dependence of the vertical shift, the same sample was used for consecutive annealing steps.

B. *Ab initio* calculations

Density functional theory (DFT) calculations were performed using the Vienna *Ab Initio* Simulation Package (VASP) [19, 20] with the generalized gradient approximation (GGA) in the Perdew, Burke, and Ernzerhof (PBE) formulation [21] and a scalar-relativistic approximation with collinear spin alignment of magnetic moments. We employed PAW potentials with the following valence states: $3p^6 3d^5 4s^2$ for Mn, $4p^6 4d^{10}$ for Pd, and $3p^6 3d^8 4s^2$ for Ni (for the comparison with Ni-Mn, see Appendix A). A supercell approach was implemented to simulate the equiatomic PdMn and Pd-excess PdMn alloys. We modeled a 432-atom supercell by repeating a 16-atom PdMn cell three times along each Cartesian axes and introduced one extra Pd atom instead of Mn in the middle of the supercell at the (0.5; 0.5; 0.5) site. Thus, the resulting composition of the defective structure is $\text{Pd}_{50.23}\text{Ni}_{49.77}$. For these two systems, we determined the lattice constants, total and site-resolved magnetic moments, and electronic densities of states (DOS). The energy cut-off for the plane wave basis set was set to 460 eV. The ionic relaxation was stopped when the change of the total energy became less than 10^{-6} eV. The conversion criterion for the electronic degrees of freedom provided an accuracy of 10^{-8} eV. The Brillouin zone was integrated with the first-order Methfessel-Paxton [22] method with a smearing parameter $\sigma = 0.1$ eV using a Monkhorst-Pack $4 \times 4 \times 4$ k -point grid. To show the effect of the increasing Pd excess on the electronic structure, we investigated the DOS of $\text{Pd}_{50.23}\text{Mn}_{49.77}$ (432 atoms) and $\text{Pd}_{56.25}\text{Mn}_{43.75}$ (16 atoms) and compare them with NiMn (Appendix A). Calculations are performed for the AF configuration depicted in Fig. 7, which is energetically favorable for PdMn [23] and NiMn alloys [24–26].

III. EXPERIMENTAL RESULTS

A. Structure

We show the refined XRD-data of the initial state of the PdMn sample in Fig. 1. The refinement was carried out with JANA2006 software [27] using the P4/mmm

space group. The lattice parameters were determined as $a = 2.88 \pm 0.01\text{Å}$ and $c = 3.60 \pm 0.01\text{Å}$, which are in agreement with reference [15]. Two additional XRD-peaks marked with arrows are present at 46° and 67.5° . These could be related to the presence of Pd_2Mn (orthorhombic) and Pd_3Mn (tetragonal) [28]. The presence of these peaks are due to the unpolished edges of the sample. This is confirmed by our EDX-measurements made on polished disks cut from the original ingot showing no inhomogeneities except at the edges. Also our magnetization measurements on the cuboids, which were cut from areas away from the edges, show no features related to Pd-rich Pd-Mn [12].

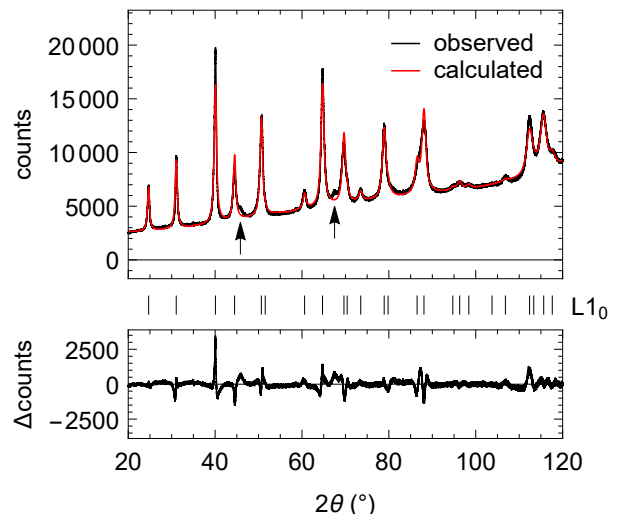


FIG. 1. Refined room-temperature XRD-measurements of the bulk PdMn sample. XRD-measurements were done directly after quenching the sample from 1073 K in room-temperature water. The measurement shows mainly the normal L1_0 -structure of PdMn. Two additional peaks (at 46° and 67.5°) are visible and marked with arrows.

B. Magnetization

1. Vertical shift in $M(B)$

We show in Fig. 2 $M(B)$ for $\text{Pd}_{52.9}\text{Mn}_{47.1}$ before and after annealing for 6 h at 650 K in 5 T. The full measurement range is shown in Fig. 2 (a). Both $M(B)$ -curves are essentially linear, which is the typical behaviour of an antiferromagnet. The magnetic susceptibility increases after magnetic annealing.

Figure 2 (b) shows the region around zero field in more detail. Here, it becomes evident that the $M(B)$ -curve is shifted vertically after magnetic annealing. In this case, the shift is $M_{\text{Shift}} = (3.1 \pm 0.4) \times 10^{-3} \text{Am}^2/\text{kg}$. The shift stems from pinned magnetic moments in the

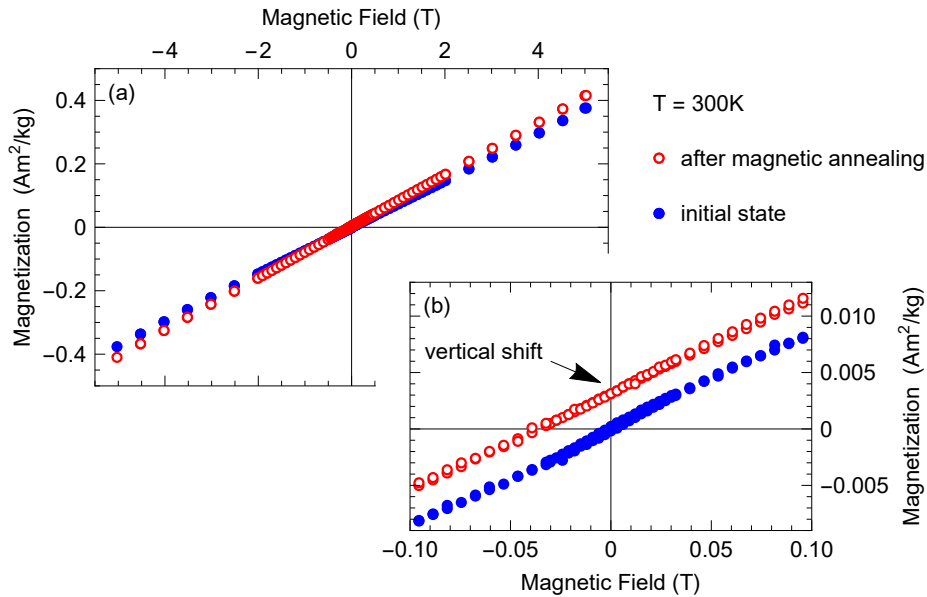


FIG. 2. (a) Field-dependent magnetization measurements of $\text{Pd}_{52.9}\text{Mn}_{47.1}$ measured at 300 K before and after magnetic annealing for 6 h at 650 K and 5 T. After annealing the $M(B)$ -curve is shifted upwards along the magnetization axis and the linear background is increased. (b) the region around zero field in more detail.

sample. A small FM component is also visible. It can be identified in Fig. 2 (b) as a S-shaped deviation from the linear dependence of the magnetization on the magnetic field.

2. Dependence of the vertical shift on the annealing field

Figure. 3 shows the dependence of the size of the vertical shift on B_a . For each data-point, a fresh initial state sample was annealed at 650 K for 6 h. For each sample, a different B_a between 0 T and 5 T was applied. The resulting vertical shift increases linearly with increasing B_a with a slope of $M_{\text{Shift}} = (6.8 \pm 1.1) \times 10^{-4} \text{Am}^2/\text{kgT}$.

3. Dependence of the vertical shift on the annealing time

Figure 4 shows the dependence of the size of the vertical shift on t_a for values of T_a of 600 K, 625 K, and 650 K. B_a is 5 T. The vertical shifts are determined from $M(B)$ curves obtained at 300 K. The t_a -dependence is measured consecutively for each T_a , and for all measurements the same sample is used.

The vertical shift for all three T_a increases with increasing t_a , while showing a tendency towards saturation. Only the time dependencies for values of T_a of 625 K and 650 K have been measured until full saturation, while for the 600 K measurement M_{Shift} does not

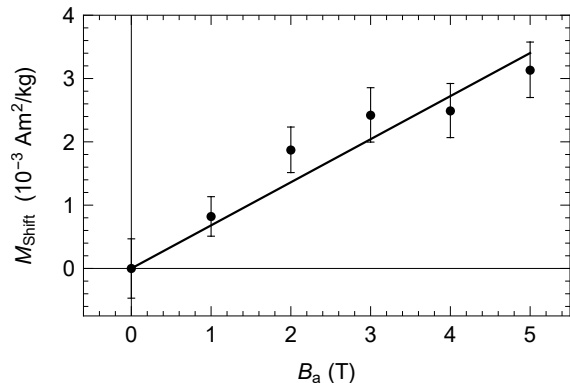


FIG. 3. B_a -dependent M_{Shift} of $\text{Pd}_{52.9}\text{Mn}_{47.1}$. $t_a = 6$ h, and the $T_a = 650$ K. B_a is varied between 0 T and 5 T. Each data-point represents a new annealing with a fresh sample. The vertical shifts are determined from $M(B)$ curves at 300 K. The solid line is a linear fit.

saturate even after 60 h. The vertical shift saturates for 625 K at $M_{\text{Shift}} = (3.6 \pm 0.24) \times 10^{-3} \text{Am}^2/\text{kg}$ and for 650 K at $M_{\text{Shift}} = (2.4 \pm 0.2) \times 10^{-3} \text{Am}^2/\text{kg}$. These values are marked with dashed lines in Fig. 4. It is apparent that the saturated vertical shift for 600 K will surpasses the values for 625 K and 650 K.

To use the same sample for every T_a , it is necessary

to do a sample-reset after each t_a -dependence. For a sample-reset, the sample is annealed without applying a magnetic field. This procedure sets the vertical shift back to zero. Since the t_a -dependence was measured at three different T_a (650 K, 625 K, and 600 K in this chronological order), two resets were done. The first was 4 h at 650 K without a magnetic field and the second was 4 h at 650 K plus 1.5 h at 700 K without magnetic field.

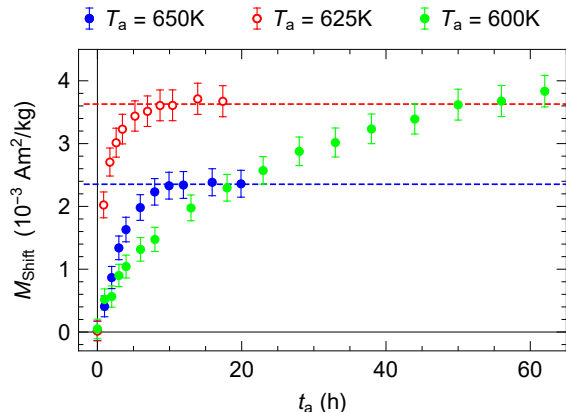


FIG. 4. t_a -dependent M_{Shift} of $\text{Pd}_{52.9}\text{Mn}_{47.1}$. B_a is 5 T. The time dependence was measured for values of T_a of 650 K, 625 K, and 600 K. For each T_a the same sample was used. After measuring the full time dependence for a certain T_a , the sample was reset. The vertical shifts were determined from $M(B)$ curves at 300 K. The dashed line marks the saturation value of the vertical shift for a certain T_a .

Such a sample-reset is shown in Fig. 5 after the first annealing procedure, which was 19.9 h at 650 K in 5 T. The measurement is divided in a temperature dependence from 300 K to 650 K with a rate of 4 K min^{-1} and a subsequent 4 h time dependence measured with a fixed temperature of 650 K. No magnetic field was applied during this measurement.

The measurement starts at room temperature. Since no magnetic field is applied, the measured value corresponds to the last measured vertical shift (blue in Fig. 4). With increasing temperature the measured magnetization increases until reaching a maximum at around 500 K. Afterwards, the magnetization decreases with increasing slope until 650 K. While staying at 650 K an exponential decay is visible until it saturates just below $0 \text{ Am}^2/\text{kg}$ after 4 h. The small negative magnetization is a result from residual currents in the superconducting magnet. We want to stress that the temperature dependence measured above 500 K represents a non-equilibrium state so the measured value is not constant in time. Staying at 550 K instead of 650 K would therefore still result in an exponential decay of the magnetization. Only the time necessary to reach equilibrium would increase. After the reset, no vertical shift can be measured in the $M(B)$ -curve anymore.

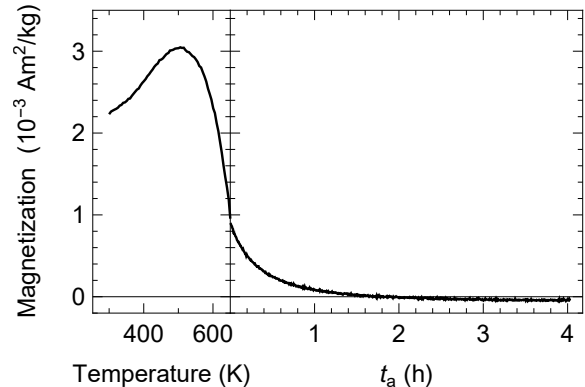


FIG. 5. Sample-reset done after annealing for 19.9 h at 650 K in 5 T. The plot shows a temperature dependent magnetization measurement with a speed of 4 K min^{-1} from 300 K to 650 K and a subsequent time dependent magnetization measurement at 650 K for 4 h all without applying a magnetic field.

4. Dependence of the vertical shift on the annealing temperature

We show in Fig. 6 the dependence of the size of the vertical shift on values of T_a between 550 K and 750 K. For each data-point a fresh initial state sample was annealed in 5 T for 6 h. A vertical shift begins to appear for T_a above 575 K and increases until it reaches a maximum at 650 K. The time dependence in Fig. 4 has shown that this increase of M_{shift} with increasing temperature is due to an increase in diffusion kinetics. This means M_{shift} below 650 K is only smaller, because it has not yet reached its equilibrium value after 6 h of annealing. Above 650 K, on the other hand, M_{shift} decreases until it vanishes for 725 K and above. This is because an increase in thermal energy counters the imbalance in the occupation of the two AF Mn-sublattices by the Pd-excess atoms and will therefore reduce the equilibrium value of M_{shift} .

IV. MODELING

In this section, we calculate the dependence of the pinned magnetization on B_a , t_a , and T_a based on the magnetic-field-biased diffusion model developed in references [7, 8] and compare it to the experimental results. For this purpose, we use the results of the *ab initio* calculations. Parameters describing the diffusion kinetics were determined experimentally and are presented in App. B.

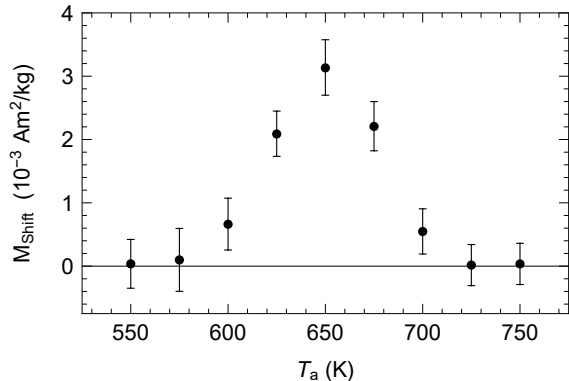


FIG. 6. T_a dependent M_{Shift} of $\text{Pd}_{52.9}\text{Mn}_{47.1}$. $t_a = 6$ h, and B_a is 5 T. T_a is varied between 550 K and 750 K. Each data-point represents a new annealing with a fresh sample. The vertical shifts are determined from $M(B)$ curves at 300 K

A. Magnetic properties determined from DFT

We performed full geometric optimization of the PdMn and Pd-excess compositions. The calculated lattice parameters of $a = 2.82 \text{ \AA}$ and $c = 3.69 \text{ \AA}$ agree with the experimental values in this work and Refs. [15, 17] and with *ab initio* calculations [23]. The obtained lattice constants are nearly the same for both ideal L1_0 -PdMn and for the structure with Pd-excess. However, the c/a ratios of these structures differ slightly, i.e., the lattice with Pd-excess is compressed in x and y and stretched in c compared to the equiatomic structure. This is associated with a change in the interatomic distances around the defect (Pd₁ atom in Fig. 7(b)). The nearest-neighbor (NN) distance of 2.82 \AA between Mn₁-Mn₆ in PdMn decreases to 2.77 \AA for NN Pd₁-Mn₆ and the distance between the Mn- and Pd-planes (along c axis) increases. The latter is related to the larger atomic size of the $4d$ Pd atom compared to the $3d$ Mn atoms in the plane. This is in contrast to the NiMn system, where introducing Ni excess atoms results in a decrease of c , due to the, compared with Mn, smaller Ni radius.

The excess Pd atom on the Mn-position also changes the magnetic environment. Calculated site-resolved and total magnetic moments of the equiatomic and Pd-excess PdMn systems are summarised in Table I. In the equiatomic composition, the Pd atoms carry no magnetic moments, while the Mn atoms each have a moment of $\pm 3.798 \mu_B$. The collinear AF configuration leads to a total magnetic moment of zero. For the Pd-excess PdMn, the Pd-excess atom in the Mn plane (Pd₁ in Fig. 7(b)) results in magnetic inhomogeneities in the vicinity of this defect. NN Mn₆ atoms surrounding the defect acquire the largest moments of the system of $3.858 \mu_B$. The moments of next-NN Mn₄ and next-next-NN Mn₃ also increase in magnitude, while Mn₅ at the distance of $\approx 4.65 \text{ \AA}$ has

the same moment as in ideal PdMn. Mn₂, which has the largest distance from the defect atom, has the, in absolute values, lowest magnetic moment, which is also slightly smaller than in the equiatomic composition. This indicates that the bulk properties are not fully reached yet, and even a 432-atom cell might not be fully sufficient to harbor the entire polarization cloud. The excess Pd atom Pd₁ acquires a moment of $0.347 \mu_B$, which is induced by the surrounding Mn atoms and parallel to the NN Mn₆. The regular Pd₂ atoms also acquire a moment of $0.03 \mu_B$. A Pd-excess atom on a Mn-position leads to an uncompensated configuration and results in a total magnetic moment of $4.977 \mu_B$. Compared to a Ni-excess atom in NiMn, where the total magnetic moment is $4.997 \mu_B$ [8], this is slightly smaller.

B. Magnetic-field-biased diffusion

1. Dependence of the vertical shift on the annealing field

The magnetic-field-biased diffusion model describes the experimentally observed vertical shift in $M(B)$ of Pd-rich PdMn with the accumulated excess Pd atoms in one of the two AF Mn-sublattices [7, 8]. The reason for this is the presence of an energy-difference between the two possible occupations of the AF Mn-sublattices in B_a . The vertical shift in $M(B)$ for a single crystal under equilibrium conditions, i.e., when sufficient time has elapsed after applying B_a , can then be calculated from

$$M_{\text{shift}} = C \tanh\left(\frac{\vec{\mu}_- \cdot \vec{B}_a}{k_B T_a}\right) \vec{\mu}_{\text{Total}} \cdot \hat{e}. \quad (1)$$

Here C is the scaling factor

$$C = \frac{1}{2} \frac{c_{\text{Pd}} - c_{\text{Mn}}}{c_{\text{Pd}} m_{\text{Pd}} + c_{\text{Mn}} m_{\text{Mn}}}, \quad (2)$$

with the atomic masses of Pd and Mn as m_{Pd} and m_{Mn} , and their atomic concentrations as c_{Pd} and c_{Mn} . This scaling factor is needed to obtain M_{shift} as the mass magnetization. We use the stoichiometry of our measured sample $\text{Pd}_{52.9}\text{Mn}_{47.1}$ for the calculations. $\vec{\mu}_{\text{Total}}$ is the magnetic moment caused by a Pd-excess atom on a Mn-position in the PdMn lattice. During diffusion mediated by mono-vacancies, which is the main diffusion mechanism at the observed temperatures, $\vec{\mu}_{\text{Total}}$ is strongly reduced. μ_- is this reduced moment. \hat{e} is a unit vector in the measurement direction, and k_B the Boltzman constant. If the magnetic moments, magnetic field and the measurement direction are parallel, the Taylor expansion of Eq. 1 becomes

$$M_{\text{shift}} = C \mu_{\text{Total}} \frac{\mu_- B_a}{k_B T_a} + \mathcal{O}\left[\left(\frac{\mu_- B_a}{k_B T_a}\right)^3\right]. \quad (3)$$

This implies that if the thermal energy is substantially larger than the Zeeman energy, a linear dependence of

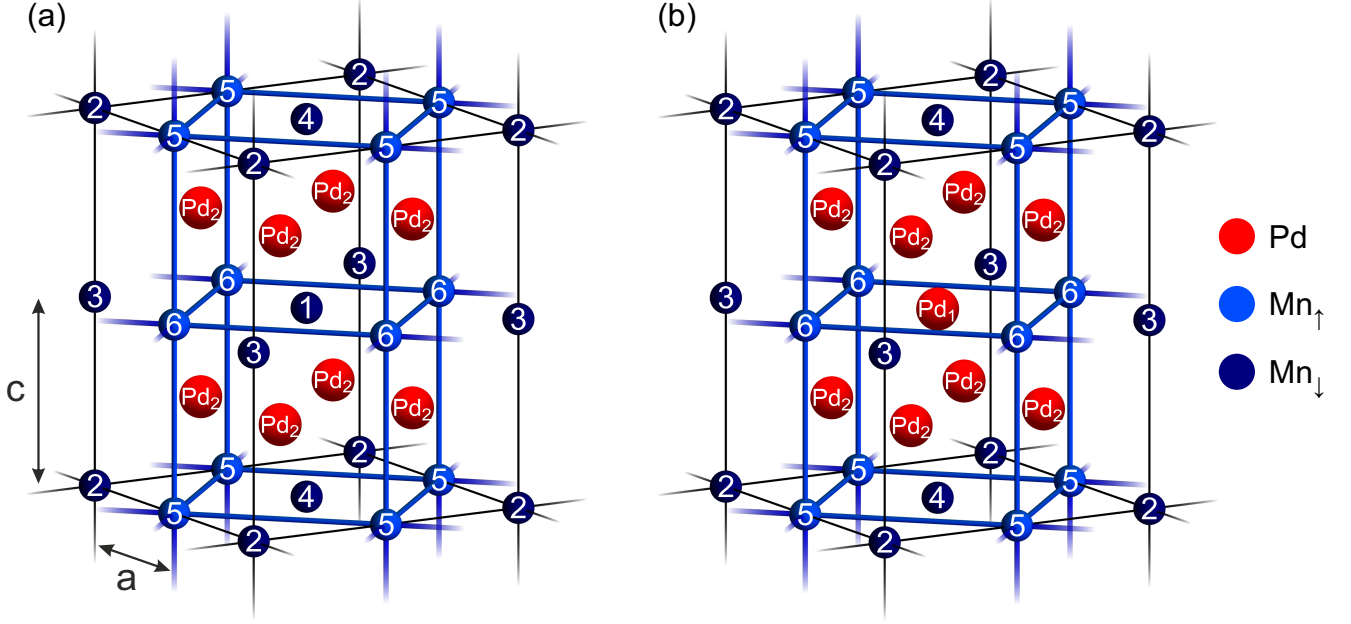


FIG. 7. (a) Equiatomic PdMn and (b) the structure where the Mn atom in the center is replaced by a Pd atom (Pd₁). This leads to the emergence of a non-zero net magnetic moment. The two AF sublattices of the Mn atoms are indicated by two different shades of blue. Supercells for the first-principles calculations are formed by a $3 \times 3 \times 3$ elongation of the 16-atom cell.

TABLE I. Site-resolved and total magnetic moments μ of ideal equiatomic PdMn and the PdMn supercell with one Pd-excess atom. The numbering of atoms corresponds to Fig. 7.

	Site-resolved μ_i (μ_B /atom)								Total μ_{Total} (μ_B)
	Mn ₁	Mn ₂	Mn ₃	Mn ₄	Mn ₅	Mn ₆	Pd ₁	Pd ₂	
w/o excess Pd	-3.798	-3.798	-3.798	-3.798	3.798	3.798	—	0.000	0.000
with excess Pd	—	-3.777	-3.814	-3.824	3.799	3.858	0.347	0.030	4.977

M_{shift} on B_a would be expected. M_{shift} for a polycrystal has to be determined by the integration of Eq. 1 on the surface of a unit hemisphere [8]. One obtains,

$$M_{\text{shift, poly}} = C \mu_{\text{Total}} \frac{\pi^2 - 12x^2 + 24x \ln(1 + \exp(2x))}{24x^2} \quad (4)$$

$$+ \frac{12\text{Li}_2(-\exp(2x))}{24x^2} = \frac{1}{3} C \mu_{\text{Total}} \frac{\mu_- B_a}{k_B T_a} + \mathcal{O} \left[\left(\frac{\mu_- B_a}{k_B T_a} \right)^3 \right], \quad (5)$$

where Li_2 is the polylogarithm of order 2. Here, we used the abbreviation

$$x = \frac{\mu_- B_a}{k_B T_a}. \quad (6)$$

For our calculations, special care has to be taken in

determining the correct values for both μ_{Total} and μ_- . μ_{Total} is taken from the *ab initio* calculations of the equiatomic defect-free structure shown in Fig. 7 (b). The corresponding value is $\mu_{\text{Total}} = 4.977 \mu_B \approx 5 \mu_B$ from Tab. I. In reality, the local environment of individual Pd-excess atoms can deviate from this structure. For example, multiple Pd-excess atoms can be in close proximity to each other or even neighbours. However, for practical purposes we choose this value for our calculations. μ_- , on the other hand, is strongly reduced with respect to μ_{Total} , because during mono-vacancy diffusion a Mn atom in Fig. 7 (b) next to the Pd-excess atom is replaced by a vacancy and changes the local magnetic environment. Therefore, we use our experimental result to determine μ_- . For this, we use the slope of the B_a -dependence of M_{shift} in Sec. III B 2, $(6.8 \pm 1.1) \times 10^{-4} \text{Am}^2/\text{kgT}$, and obtain $\mu_{\text{Total}} \times \mu_- = (1.0 \pm 0.2) \mu_B^2$. We can divide this value by μ_{Total} to obtain $\mu_- = 0.2 \mu_B$. These values for μ_{Total} and

μ_- will be used in further calculations.

We show in Fig. 8 the calculated B_a -dependence of M_{shift} at $T_a = 650$ K. The results for both single crystals and polycrystals are plotted. In all calculations for single crystals, the magnetic field is parallel to the direction of the AF alignment. Figure 8 (a) is plotted up to very high hypothetical magnetic fields to show the saturation behaviour of M_{shift} in Eq. 1 and Eq. 4. In Fig. 8 (b) we see the same calculations in fields up to 5 T. This result is the calculated counterpart of the experimental result shown in Fig. 3 and shows the appropriateness of the linear approximation. It is noteworthy that for small magnetic fields, M_{shift} for a polycrystal is a third of the value for that of a single crystal (Fig. 8 (b)), while for large magnetic fields it becomes a half of the value (Fig. 8 (a)).

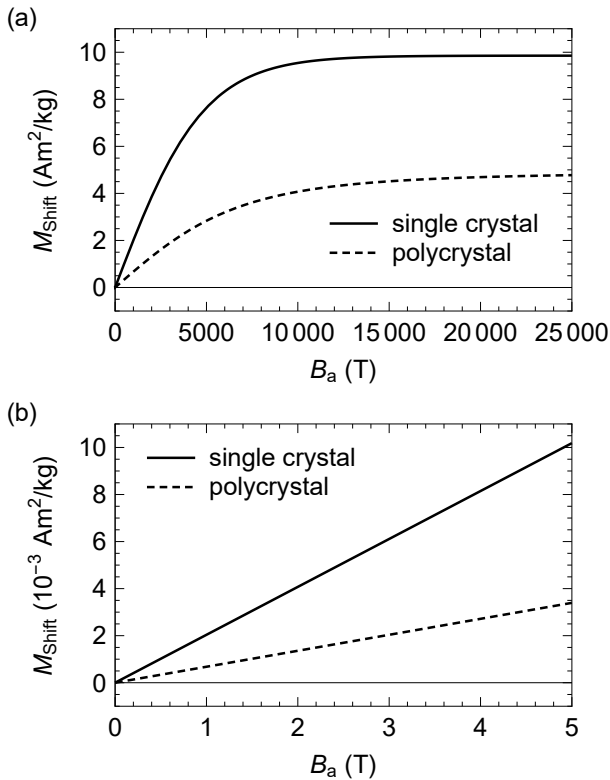


FIG. 8. Annealing field dependence of the vertical shift calculated for a single crystal and a polycrystal. (a) dependence up to saturation at very high hypothetical magnetic fields. (b) dependence on magnetic fields up to 5 T. For the calculations $T_a = 650$ K.

2. Dependence of the vertical shift on the annealing time

To determine the t_a -dependence expected from the magnetic-field-biased diffusion model, one has to consider the rate equations. The total amount of Pd-excess atoms

$N = N_- + N_+$ is a fixed number. N_- and N_+ are defined as the number of Pd-excess atoms in the sublattice with a minimized and maximized Zeeman-energy. At any point, a Pd-excess atom can change from N_- to N_+ and vice versa. This means that the diffusion process can be treated as a reversible reaction with unequal rates. With the corresponding diffusion rates ω_- and ω_+ , which are given as

$$\omega_{\pm} = \Gamma_0 \exp\left(-\frac{(A_0 \mp 2 \vec{\mu}_- \cdot \vec{B}_a)}{k_B T_a}\right), \quad (7)$$

one can write the rate equations as

$$\frac{dN_-}{dt_a} = \omega_+ N_+ - \omega_- N_- \quad (8)$$

and

$$\frac{dN_+}{dt_a} = \omega_- N_- - \omega_+ N_+. \quad (9)$$

Here Γ_0 is the attempt frequency and A_0 the activation energy without applied field. These differential equations can be solved by separating the variables to obtain $N_-(t_a)$ and $N_+(t_a)$. The initial conditions are $N_-(0) = N_+(0) = N/2$. The t_a -dependence of M_{shift} is then described by $\Delta N(t_a) = N_-(t_a) - N_+(t_a)$. Multiplying this with the scaling factor and the scalar product of $\vec{\mu}_{\text{Total}}$ and \hat{e} gives the t_a -dependent magnetization as

$$M_{\text{shift}}(t_a) = C \tanh\left(\frac{\vec{\mu}_- \cdot \vec{B}_a}{k_B T_a}\right) \left(1 - \exp(-(\omega_- + \omega_+) t_a)\right) \vec{\mu}_{\text{Total}} \cdot \hat{e}. \quad (10)$$

Under experimental conditions, the Zeeman term in Eq. 7 is much smaller than the activation energy of diffusion. It can thus be neglected in calculation of $M_{\text{shift}}(t_a)$ so that,

$$\omega_- + \omega_+ \approx 2 \omega_0 = 2 \Gamma_0 \exp\left(-\frac{A_0}{k_B T_a}\right). \quad (11)$$

With these assumptions, we obtain $\Gamma_0 = 1 \times 10^{14} \text{ s}^{-1}$ and $A_0 = 2.3 \text{ eV}$ (App. B) using our experimental results.

We show in Fig. 9 the calculated t_a -dependencies of M_{shift} . In Fig. 9 (a), we compare the results for single crystals and for polycrystals at $T_a = 650$ K and $B_a = 5$ T. In Fig. 9 (b) we show the t_a -dependence of M_{shift} for the three temperatures 600 K, 625 K and 650 K. With higher temperature, the rate of increase of M_{shift} increases with higher T_a , while the saturation value of M_{shift} decreases. This is the calculated counterpart of the experimental result shown in Fig. 4.

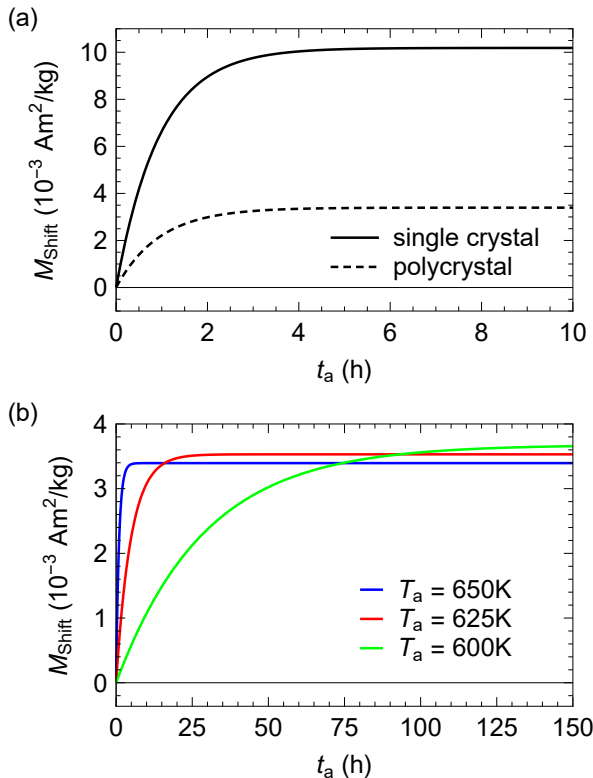


FIG. 9. t_a -dependence of the vertical shift calculated for a single crystal and a polycrystal with $B_a = 5 \text{ T}$. (a) t_a -dependence at $T_a = 650 \text{ K}$. (b) t_a -dependence of a polycrystal at values of T_a of 600 K, 625 K and 650 K.

3. Dependence of the vertical shift on the annealing temperature

The dependence of M_{shift} on T_a can be calculated in the same way as the dependence of M_{shift} on B_a using Eq. 1 and Eq. 4.

We show in Fig. 10 the calculated temperature dependence of M_{shift} for $B_a = 5 \text{ T}$ for a single crystal and a polycrystal. Figure 10 (a) shows M_{shift} in the temperature range $0.1 \text{ K} \leq T_a \leq 1000 \text{ K}$ in a log-log plot. Here, the inverse proportionality of M_{shift} on T_a for temperatures higher than 1 K is visible, which is a result of the dominating term in the Taylor series expansions shown in Eq. 3 and Eq. 5. For lower temperatures, M_{shift} for both single crystals and polycrystals saturates at values equal to their respective saturation values in Fig. 8 (a). This corresponds to a full occupation of Pd-excess atoms in one of the AF sublattices. This can only be achieved by annealing at very high fields or at very low temperatures. At high T_a , M_{shift} for a polycrystal is a third of the value of that for a single crystal. At low T_a , it is a half. This behavior is the opposite of that observed for the dependence of M_{shift} on B_a .

In Fig. 10 (a), M_{shift} only at equilibrium conditions

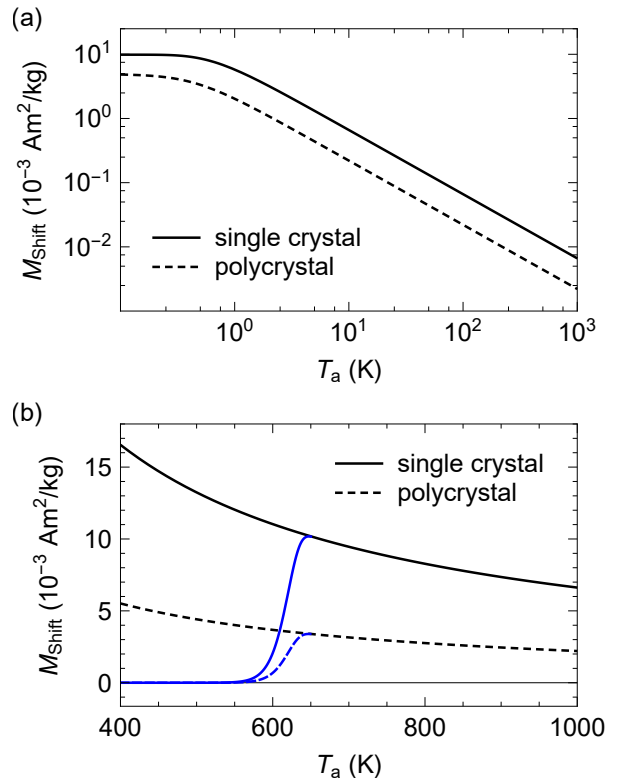


FIG. 10. Annealing temperature dependence of the vertical shift calculated for a single crystal and a polycrystal in $B_a = 5 \text{ T}$. (a) log-log plot of the vertical shift in equilibrium. (b) plot of the vertical shift in equilibrium (black) and in an intermediate state after 6 h of annealing (blue).

is plotted. In an experiment, t_a is finite and thus equilibrium at lower T_a with small diffusion rates cannot be achieved. This means that the dependence of M_{shift} on T_a obtained in an experiment will always deviate from the result calculated for equilibrium. To account for this, M_{shift} has to be calculated for an intermediate state after a finite t_a using Eq. 10. Figure 10 (b) shows the T_a -dependence of M_{shift} in a temperature range between 400 K and 1000 K for both the equilibrium value ($t_a \rightarrow \infty$, black) and an intermediate state ($t_a = 6 \text{ h}$, blue). Again, both the results for a single crystal and a polycrystal are shown. This is the calculated counterpart of the experimental result shown in Fig. 6. The decrease of M_{shift} below 650 K is also visible from the experimental results (Fig. 6 and the connection to decreased diffusion rates is confirmed by our t_a -dependent measurements in Sec. III B 3. The decrease of M_{shift} with increasing T_a above 650 K, on the other hand, is much stronger than the calculated inverse proportional dependence on T_a and is also observed in the t_a -dependent measurements.

V. CONCLUSIONS

Magnetic annealing of PdMn with excess Pd leads to strongly pinned uncompensated magnetic moments, which are noticeable as a vertical shift in $M(B)$. A model to explain this phenomenon is the magnetic-field-biased diffusion model, which was introduced within the context of studies on the magnetic properties of NiMn [7, 8]. The vertical shift in PdMn is of the same magnitude as for NiMn.

We measured the annealing time, temperature and field dependence of the vertical shift in $M(B)$ of $\text{Pd}_{52.9}\text{Mn}_{47.1}$ and compared the results with those of the magnetic-field-biased diffusion model. For this we used *ab initio* calculations and determined the magnetic moment caused by a Pd-excess atom on a Mn position as $4.977 \mu_B$. This includes the absent moment of the replaced Mn atom, which would have pointed in the opposite direction, the induced moment of the Pd-excess atom itself, and minor contributions from the surrounding magnetic environment. This is close to the previously discussed case of NiMn [8]. We confirm a good agreement between model and experiment. However, the model deviates from the experimental results for T_a higher than 650 K.

ACKNOWLEDGMENTS

We acknowledge funding by the German Research Foundation (DFG) within the Collaborative Research Center/Transregio (CRC/TRR) 270 (Project-No. 405553726, subprojects A04 and B06). The authors gratefully acknowledge the computing time provided to them at the NHR Center NHR4CES at TU Darmstadt (project number p0020039). This is funded by the Federal Ministry of Education and Research, and the state governments participating on the basis of the resolutions of the GWK for national high performance computing at universities (www.nhr-verein.de/unsere-partner). We thank Ulrich Nowak (University of Konstanz) and Alfred Hucht (University of Duisburg-Essen) for helpful discussions.

Appendix A: Effect of Pd excess on the electronic structure

To get a better understanding of the differences between PdMn and NiMn, we calculated total and partial electronic DOS of the equiatomic AF $L1_0$ -PdMn and the structure with Pd excess and compare them with the analogous structures of NiMn, which have the same AF configuration. The total DOS profile of PdMn (Fig. 11(a)) agrees with the calculation in Ref. [17]. For both ideal and defective structures, the peak at ≈ -2.5 eV is formed by strong Pd-Mn hybridization with equal contributions from Mn and Pd atoms. The two

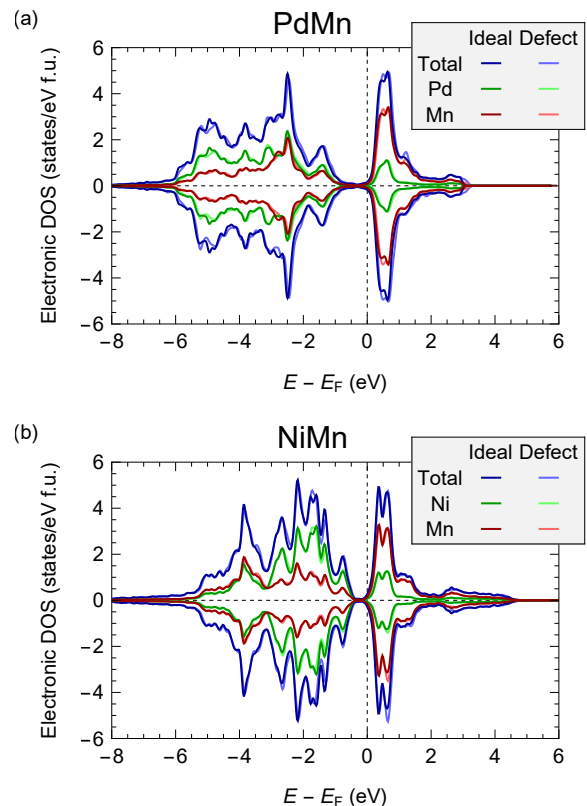


FIG. 11. Total and element-resolved electronic DOS of (a) PdMn and (b) NiMn in comparison with corresponding defective structures. Results are obtained for 432-atom supercells and normalized to 2 atoms. Defective structures contain one extra Pd/Ni atom introduced in the middle of the supercell (see the detailed description in Sec. II B).

lower features at ≈ -3.9 and -4.9 eV have an almost twice as large contribution from Pd, which can be attributed to the larger number of valence electrons of Pd. The latter peak (-4.9 eV) shows the most noticeable difference between the equiatomic and Pd-excess structure, since it is replaced by a local minimum at -5 eV in the Pd-excess structure. Both Pd systems are characterised by a deep minimum in the DOS around the Fermi level E_F forming a pseudogap. This has been reported previously for $L1_0$ -type ordered Mn_{1-x}Z , where $Z = \text{Ni}$ [24], Pt [29], and Pd [18, 29, 30]. Passing from Pd- to Ni-systems results in the narrowing of this pseudogap from 1.17 eV to 0.58 eV.

Of particular interest for us is, how further increasing the defect concentration would affect the electronic structure. Therefore, we additionally performed the full relaxation of a system with 6.25 at.% Pd excess. We found a similar trend as obtained by Umetsu *et al.* [30], who used a tight-binding linear muffin-tin orbital (LMTO) method with the coherent potential approximation (CPA), which does not involve lattice relaxation. Counterintuitively, the changes cannot simply be described by the rigid band

model, where the additional d -electrons shift the Fermi level E_F and increasing Pd-excess would be expected to shift the Fermi level into the larger peak above the pseudogap. However, The calculation shows that weight from the unoccupied DOS is redistributed below the pseudogap, and E_F finally locates at the bottom edge of the gap. As a consequence, the occupied $3d$ states move in total closer to the Fermi level, which is associated with an increase in band energy. We speculate that this suppresses clustering of the excess Pd when the overall Pd concentration is low enough to keep E_F close to the upper edge of pseudogap and, therefore, supports the field-induced diffusion of the excess-Pd atoms. The situation is similar to NiMn, where the pseudogap is, however, two times smaller.

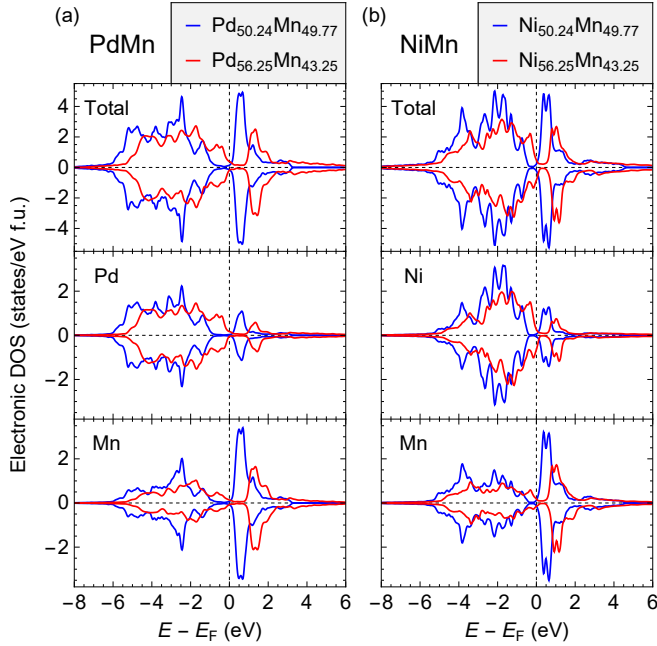


FIG. 12. Total (first row) and element-resolved (second and third rows for Pd/Ni and Mn, correspondingly) electronic DOS of Pd-Mn (left panel) and Ni-Mn (right panel). Passing from smaller (blue curves) to larger (red curves) Pd/Ni-excess content, increasing of valence electron concentration results in shifting of the whole DOS weight towards higher energies pushing the pseudo-gap above the Fermi level.

Appendix B: Diffusion kinetics

For modeling the t_a - and T_a -dependence of M_{shift} , the attempt frequency Γ_0 and the activation energy A_0 are needed. An estimation of these values can be obtained from our t_a -dependent measurements of M_{shift} . In total, we measured five t_a -dependencies, which are discussed in Sec. III B 3. If the Zeeman-contribution is neglected,

these t_a -dependencies can all be described by,

$$\Delta M_{\text{shift}}(t_a, T_a) = \exp\left(\left[-2\Gamma_0 \exp\left(-\frac{A_0}{k_B T_a}\right)\right] t_a\right). \quad (\text{B1})$$

ΔM_{shift} is the normalized difference in pinned magnetization between intermediate and equilibrium states. If the t_a -dependence is exponential, then the natural logarithm of ΔM_{shift} should depend linearly on t_a . This

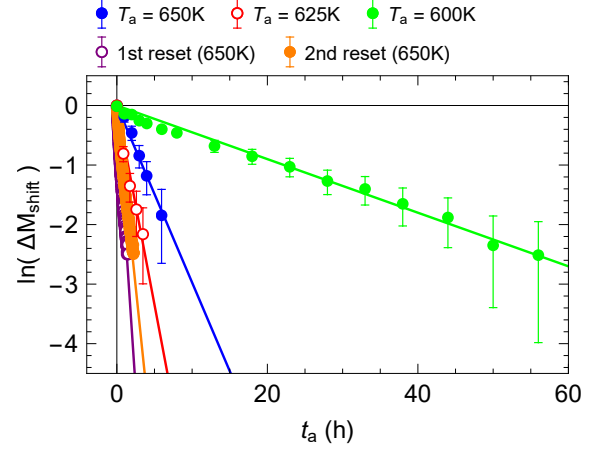


FIG. 13. The natural logarithm of ΔM_{shift} for three T_a plotted against t_a . A linear dependence indicates an exponential t_a -dependence of ΔM_{shift} . The respective linear fits are shown in the same color as the data-points.

dependence is shown in Fig. 13. Following Eq. B1, the slopes of $\ln(\Delta M_{\text{shift}})$ should become steeper with increasing T_a . Here, $T_a = 650$ K is an outlier, which does not follow this rule. This could be associated with the sequential order of the chosen T_a . In the experiments, $T_a = 650$ K was measured first, followed by $T_a = 625$ K and $T_a = 600$ K. This means that the reduced diffusion rate at $T_a = 650$ K could be caused by lattice relaxations or the release of stress inside the sample during the first annealing. We, therefore, do not take this measurement into account when determining the attempt frequency and the activation energy. The slopes of the linear fits shown in Fig. 13 correspond to the factor in front of t in Eq. B1. The natural logarithm of the slopes, multiplied by -1 , then gives $\ln(\Gamma_0) - A_0/k_B T_a$, which can be plotted against $1/T_a$. The results can be seen in Fig. 14. Again, the value for the first annealing at $T_a = 650$ K is an outlier. Γ_0 and A_0 can now be determined by a linear fit excluding this point. We obtain $\Gamma_0 = 1 \times 10^{14} \text{ s}^{-1}$ and $A_0 = 2.3 \text{ eV}$. No error is given since this is just an estimation. We now compare these results with those in the literature. In magnetic-field-biased diffusion of NiMn, an activation energy of $A_0 = 1.8 \text{ eV}$ was determined [7], which is in the same range as our result. In reference [31], the diffusion coefficient of pure palladium is found to be

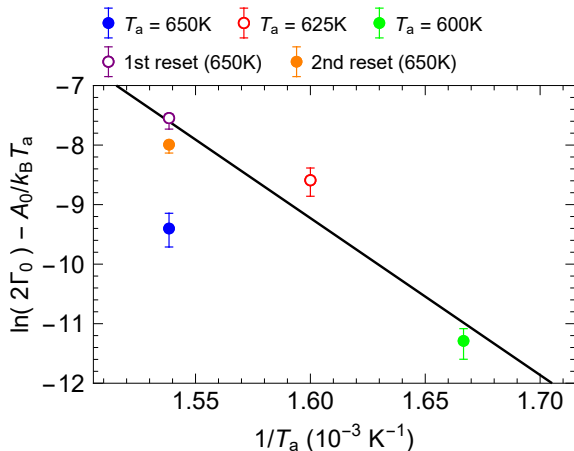


FIG. 14. $\ln(\Gamma_0) - A_0/k_B T_a$ plotted against $1/T_a$. The solid line is a linear fit from which Γ_0 and A_0 can be determined.

$D_0 = 0.205 \text{ cm}^2 \text{ s}^{-1}$. This value has to be translated into an attempt frequency by calculating

$$\Gamma_0 = \frac{D_0}{f a_{\text{Pd}}^2}. \quad (\text{B2})$$

Here, f is the correlation factor, which is 0.7815 for vacancy diffusion and a_{Pd} is the lattice parameter of Pd. This results in $\Gamma_0 = 1.7 \times 10^{14} \text{ s}^{-1}$, which is also of the same magnitude as our result.

-
- [1] J. Kasper and B. Roberts, Antiferromagnetic structure of α -manganese and a magnetic structure study of β -manganese, *Physical Review* **101**, 537 (1956).
- [2] T. Yamada, Magnetism and crystal symmetry of α -Mn, *Journal of the Physical Society of Japan* **28**, 596 (1970).
- [3] K. Binder and A. P. Young, Spin glasses: Experimental facts, theoretical concepts, and open questions, *Reviews of Modern physics* **58**, 801 (1986).
- [4] F. Heusler, Über magnetische manganlegierungen, *Verh. Dtsch. Phys. Ges* **5**, 219 (1903).
- [5] K. Fukamichi, R. Umetsu, A. Sakuma, and C. Mitsumata, Magnetic and electrical properties of practical antiferromagnetic mn alloys, *Handbook of magnetic materials* **16** (2006).
- [6] A. Berkowitz and K. Takano, Exchange anisotropy—a review, *Journal of Magnetism and Magnetic materials* **200**, 552 (1999).
- [7] L. Pál, T. Tarnóczy, and G. Konczos, Magnetic susceptibility anomaly in nearly equiatomic MnNi alloys, *physica status solidi (b)* **42**, 49 (1970).
- [8] N. Josten, O. Miroshkina, S. Noorzayee, B. Zingsem, A. Çakır, M. Acet, U. Wiedwald, M. Gruner, and M. Farle, Emergence of net magnetization by magnetic-field-biased diffusion in antiferromagnetic $L1_0$ NiMn, *arXiv preprint arXiv:2302.13387* (2023).
- [9] J. Crangle and W. Scott, Dilute ferromagnetic alloys, *Journal of applied physics* **36**, 921 (1965).
- [10] L. Vitos, B. Johansson, and J. Kollár, Size-dependent paramagnetic-ferromagnetic phase transition in palladium clusters, *Physical Review B* **62**, R11957 (2000).
- [11] M. Hansen, *Constitution of Binary Alloys*, *Materials Science and Engineering Series*, (1958).
- [12] G. Grube and O. Winkler, Magnetische susceptibilität und zustandsdiagramm bei binären legierungen.: 2. mitteilung das system palladium-mangan, *Zeitschrift für Elektrochemie und angewandte physikalische Chemie* **42**, 815 (1936).
- [13] A. Kjekshus, R. Møllerud, A. Andresen, and W. Pearson, Equiatomic transition metal alloys of manganese: VI. structural and magnetic properties of Pd-Mn phases, *Philosophical Magazine* **16**, 1063 (1967).
- [14] E. Krén and J. Sólyom, Neutron diffraction study of MnPd, *Physics Letters* **22**, 273 (1966).
- [15] L. Pál, E. Krén, G. Kádár, P. Szabó, and T. Tarnóczy, Magnetic structures and phase transformations in Mn-based CuAu-I type alloys, *Journal of Applied Physics* **39**, 538 (1968).
- [16] R. Umetsu, K. Fukamichi, and A. Sakuma, Electrical and calorimetric evidences of a pseudo-gap in antiferromagnetic equiatomic MnPd alloy, *Journal of magnetism and magnetic materials* **239**, 530 (2002).
- [17] J.-F. Wang, W.-Z. Chen, Z.-Y. Jiang, X.-D. Zhang, and L. Si, Structural, elastic, phonon and electronic properties of a MnPd alloy, *Chinese Physics B* **21**, 077102 (2012).
- [18] R. Umetsu, A. Sakuma, and K. Fukamichi, Magnetic anisotropy energy of antiferromagnetic $L1_0$ -type equiatomic Mn alloys, *Appl. Phys. Lett.* **89**, 052504 (2006).
- [19] G. Kresse and J. Furthmüller, Efficient iterative schemes for *ab initio* total-energy calculations using a plane-wave basis set, *Phys. Rev. B* **54**, 11169 (1996).
- [20] G. Kresse and D. Joubert, From ultrasoft pseudopotentials to the projector augmented-wave method, *Phys. Rev. B* **59**, 1758 (1999).
- [21] J. P. Perdew, K. Burke, and M. Ernzerhof, Generalized Gradient Approximation Made Simple, *Phys. Rev. Lett.* **77**, 3865 (1996).
- [22] M. Methfessel and A. Paxton, High-precision sampling for brillouin-zone integration in metals, *Physical Review B* **40**, 3616 (1989).
- [23] H. Yamada, H. Shimizu, K. Yamamoto, and K. Uebayashi, Structure and magnetism of 3d and 4d transition-metal alloys TT' ($T=\text{Mn, Fe}$ and $T'=\text{Rh, Pd}$) with CuAu-I type ordered structure, *Journal of alloys and compounds* **415**, 31 (2006).

- [24] A. Sakuma, Electronic structures and magnetism of CuAu-type MnNi and MnGa, *Journal of magnetism and magnetic materials* **187**, 105 (1998).
- [25] P. Entel, A. Dannenberg, M. Siewert, H. C. Herper, M. E. Gruner, V. D. Buchelnikov, and V. A. Chernenko, Composition-dependent basics of smart Heusler materials from first-principles calculations, in *Materials Science Forum*, Vol. 684 (Trans Tech Publ, 2011) pp. 1–29.
- [26] V. Sokolovskiy, M. Gruner, P. Entel, M. Acet, A. Çakır, D. Baigutlin, and V. Buchelnikov, Segregation tendency of Heusler alloys, *Physical Review Materials* **3**, 084413 (2019).
- [27] V. Petříček, M. Dušek, and L. Palatinus, Crystallographic computing system jana2006: general features, *Zeitschrift für Kristallographie-Crystalline Materials* **229**, 345 (2014).
- [28] R. Miida, T. Tajima, D. K. Saha, M. Y. Wey, D. Watanabe, and K.-i. Ohshima, Ordered structures and partial phase diagram of Pd-rich palladium-manganese alloys studied by electron diffraction and microscopy, *Materials transactions* **45**, 2822 (2004).
- [29] M. Kubota, K. Ono, R. Y. Umetsu, H. Akinaga, A. Sakuma, and K. Fukamichi, Pseudogap formation in MnPt and MnPd alloys, *Applied Physics Letters* **90**, 091911 (2007).
- [30] R. Y. Umetsu, K. Fukamichi, and A. Sakuma, Effective exchange constant and electronic structure of pseudogap-type L1₀-MnPd Alloys, *Journal of the Physical Society of Japan* **75**, 104714 (2006).
- [31] N. Peterson, Isotope effect in self-diffusion in palladium, *Physical Review* **136**, A568 (1964).